Title
Short wave Infrared Hyperspectral Camera Design based on Plasmonically Enhanced Nanowire Focal Plane Arrays

Author
Hung, Chung Hong

Publication Date
2013

Peer reviewed|Thesis/dissertation

UNIVERSITY OF CALIFORNIA

Los Angeles

Short wave Infrared Hyperspectral Camera Design

based on Plasmonically Enhanced Nanowire Focal Plane Arrays

A thesis submitted in partial satisfaction

of the requirements for the degree Master of Science

in Electrical Engineering

by

Chung Hong Hung

2013

ABSTRACT OF THE THESIS

Short wave Infrared Hyperspectral Camera Design

based on Plasmonically Enhanced Nanowire Focal Plane Arrays

by

Chung Hong Hung

Master of Science in Electrical Engineering

University of California, Los Angeles, 2013

Professor Diana L. Huffaker, Chair

State-of-art short wave infrared hyperspectral cameras use filters for sorting photons which lead to ineffective use of incoming light and/or longer recording time. This work proposes a hyperspectral camera design that eliminates the need of a filtering layer and promises over 50% reduction in pixel size. The significant size reduction is attributed from the use of surface plasmon resonances, which enhances optical collection area and enables photon sorting below

the diffraction limited spot size unlike conventional methods. Absorbed photons are then guided into nanowire absorbers. Compared to planar absorbers, a nanowire absorber allows three-dimensional absorption volume, while at the same time reduces capacitance and lowers the dark current. The performance of the designed structure is modeled, showing selective absorption at 1050, 1250, and 1550 nm for short wave infrared applications.

The thesis of Chung Hong Hung is approved.

Benjamin Williams

Robert N. Candler

Diana L. Huffaker, Committee Chair

University of California, Los Angeles

2013

Table of Contents

List of Acronyms

3D	Three dimensional
APD	Avalanche photodiode
CAD	Computer-aided design
EM	Electromagnetic
EOT	Extraordinary optical transmission
FDTD	Finite-difference time-domain
FPA	Focal plane array
InGaAs	Indium Gallium Arsenide
IR	Infrared
LSP	Localized surface plasmon
MCT/HgCdTe	Mercury Cadmium Telluride
PEPD	Plasmonically-enhanced photodetector
PML	Perfectly matching layers
QE	Quantum efficiency
ROIC	Read-out integrated circuit
SNR	Signal-to-noise ratio
SPP	Surface plasmon polariton
SWaP	Size, weight, and power
SWIR	Shortwave infrared
wd	Wire diameter
xh	Exposed height
λ	Wavelength

1 Introduction

1.1 Why short-wave infrared hyperspectral camera?

While infrared light is invisible to human eye, short-wave infrared (SWIR) is mostly reflective in nature, bouncing off of objects much like visible light. As opposed to mid-wave and long-wave IR imaging based on thermal radiation given off from hot objects, images produced by reflective SWIR cameras are usually much easier to perceive and are comparable to visible light imagery. This gives rise to a range of applications for SWIR cameras, such as visual penetration through fog and smoke and night glow imaging. Compared to cameras in other wavelength of the electromagnetic (EM) spectrum, SWIR cameras are still relatively new in the camera market [1–4].

Most SWIR cameras employ the hyperspectral imaging technology. Similar to the human eye, which sees visible light in red, green, and blue bands, SWIR hyperspectral imaging breaks down the SWIR spectrum (0.9 – 1.7 μm) into multiple sub-bands. Information of the incoming light is processed based on the intensities and the ratios of the sub-bands. To do so, cameras use focal plane arrays (FPAs) to capture light and convert it into electrical signal for further processing in a read-out integrated circuit (ROIC) [5,6]. Ideally, each pixel in the FPA has to be able to split the incoming light into several sub-bands for detection. Traditional photodetectors do so often by using filters or interferometers combined with scanning or subsampling to record a spectral image 'cube' (with wavelength as the third dimension) [7,8]. This often leads to inefficient use of the incoming light and/or results in longer recording time.

1.2 State-of-art work

Recently, a new type of filtering technology has enabled direct recording of spectral image cubes in a single exposure by sorting photons [9–11]. Using volume Bragg gratings to trap light waves on the metal/dielectric interface, surface plasmon resonances can be excited, effectively sorting and guiding incoming photons to desired location for photoabsorption (Appendix A). This type of plasmonically enhanced filter ensures both high spectral and spatial resolution, significantly increases sensitivity compared to other competing technologies such as push broom spectrometer, liquid crystal tunable filters, or acousto-optic tunable filters [12,13].

By texturing metal surfaces at the nanoscale to form gratings, incoming light can be sorted into different wavelengths based on the surface plasmon resonances. Indications that these concepts could be applied to the SWIR regime were further encouraged by the observation of extraordinary optical transmission (EOT) of light through periodic arrays of sub-wavelength holes/slits in a metal film [14–18] or a sub-wavelength aperture surrounded by periodic bullseye pattern [19,20]. This phenomenon is accompanied by a significant enhancement of the electric field within the subwavelength aperture, which can be leveraged for a variety of photonic applications.

The two most common absorber materials used in SWIR detectors are Mercury Cadmium Telluride (HgCdTe/MCT) and Indium Gallium Arsenide (InGaAs). Both materials can be engineered to tune their optical absorption to the desired wavelength. Due to their high sensitivity and high electrical mobility, few other materials exceed their performances in SWIR detection. The two main parameters for a detector are the quantum efficiency (QE) and the dark current. In terms of the QE, both materials are capable of sensing down to single photon using an avalanche photodiode (APD) approach [21–24]. HgCdTe based detectors however, suffer heavily

from thermal noise unless operated in cooled temperature, limiting their use in portable devices due to requirement of heavy and bulky cooling units [25]. In contrast, InGaAs based detectors are able to operate in much higher temperature without sacrificing its performance [26–28]. This work will focus on the use of InGaAs as the absorber material.

1.3 Proposed device design

Presented in this work is an innovative design to further modify the existing plasmonically enhanced filter by placing a nanowire photodetector next to the subwavelength aperture. The design schematic and scanning electron microscopy (SEM) images of a fabricated FPA are shown in Fig. 1 to prove the practicality of the design. The nanowire absorber is grown by metalorganic chemical vapor deposition (MOCVD) using a patterned SiO_2 mask, and the subwavelength apertures are self-aligned to the nanowires by an angled metal deposition (Appendix B). This design modification has several substantial advantages: 1) it combines the

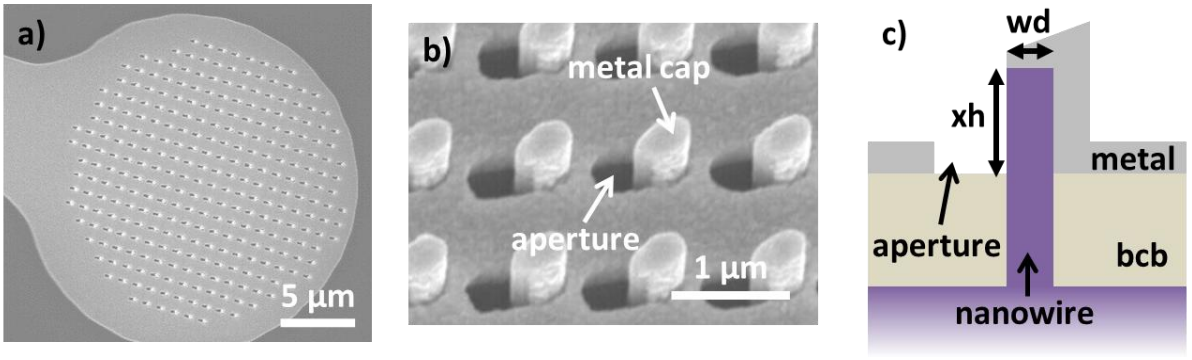

Figure 1 a,b) SEM images from an array of fabricated devices showing uniformity of the nanowires in the array. Subwavelength apertures are self-aligned to the nanowires by an angled metal deposition using the nanowires as the shadow masks. **c)** Schematic of a side view of the nanowire. The wire diameter (*wd*) and the exposed height (*xh*) are two important parameters in controlling the surface plasmon resonances of the nanowire.

plasmonic filtering layer with the photoabsorbing layer, which eliminates the need to focus or align the apertures with the detectors underneath, 2) harvesting photons becomes more direct with the enhanced field close to the nanowire detector, 3) the metal used for sustaining surface plasmon resonances can also be conveniently used as the electrical contact, and 4) the nanowire provides a shadow mask for self-aligned aperture using an angled metal deposition, avoiding any need of sophisticated lithography techniques (Appendix B).

In general, the benefit of using a plasmonically enhanced photodetector (PEPD) is that the large collection area of light can be concentrated onto a much smaller volume – in this case a photodiode junction area in a nanowire. The use of nanowire as the photoabsorber is a very attractive route for photodetectors. The miniaturization of volume significantly reduces capacitance and dark current compared to planar detectors. In terms of optical absorption, surface plasmon enhancement in planar detectors is often limited by the shallow penetration depth of the electric field intensity into the absorption region. In contrast, the three-dimensional (3D) absorption surface area of nanowires allows for greater absorbing volume enhancing light collection and absorption [29].

The 3D absorption surface of the nanowire enables various field enhancement mechanisms to be leveraged, including the resonant field enhancement occurring in bounded metallic/dielectric structures that support localized surface plasmon (LSP), and the enhancement near the metal/dielectric interface in a propagating surface plasmon polariton (SPP) mode (Appendix A). These resonant field "focusing" effects effectively increase the optical path length to be many times larger than the physical junction thickness. In principle, this allows the reduction of the detector volume even below the diffraction limit resulting in more efficient

integration, reduced pixel size, material growth requirements, and higher signal-to-noise ratio (SNR). However, detectors operating in the near infrared range are spectrally close to the plasma resonances of noble metals resulting in ohmic absorption losses. These losses need to be quantified and reduced for realizing high efficiency PEPDs.

2 Camera design

2.1 Design concept

The goal of this work is to develop a SWIR hyperspectral camera pixel design. The pixel will have to be able to sort the incoming photons into three sub-bands centered at 1050, 1250, and 1550 nm, a choice justified by the spectral intensity peaks of night glow. Three types of InGaAs nanowire absorbers will be present in a pixel, each responsible to absorb one of the sub-bands. The flow of the optimization process of the detector can be broken down as followings:

1) optimize LSP resonances for each nanowire detector for optical absorption at wavelength (λ) = 1050, 1250, and 1550 nm,

2) design gratings to further enhance the absorption through a hybrid SPP-LSP mode, and

3) arrange the three detectors into a square pixel.

Commercialized Maxwell solver software Lumerical using finite-difference time-domain (FDTD) method will be employed for the computer-aided design (CAD) of the optimized structure. The simulation is composed of (i) a simulation region box, (ii) an illuminating source, (iii) the device structure, and (iv) a monitor to record electric field (Fig. 2). Each component of the simulation is set as follows:

(i) The simulation region box defines the size of the simulation region, the boundary condition of the region edges, and the mesh settings. For LSP simulation (section 2.2), the size of the simulation region is 2.5 µm × 2.5 µm, which is typically large enough to model an isolated device performance, and the boundary condition is set as perfectly matching layers (PML), which absorb EM energy incident upon them, imitating a

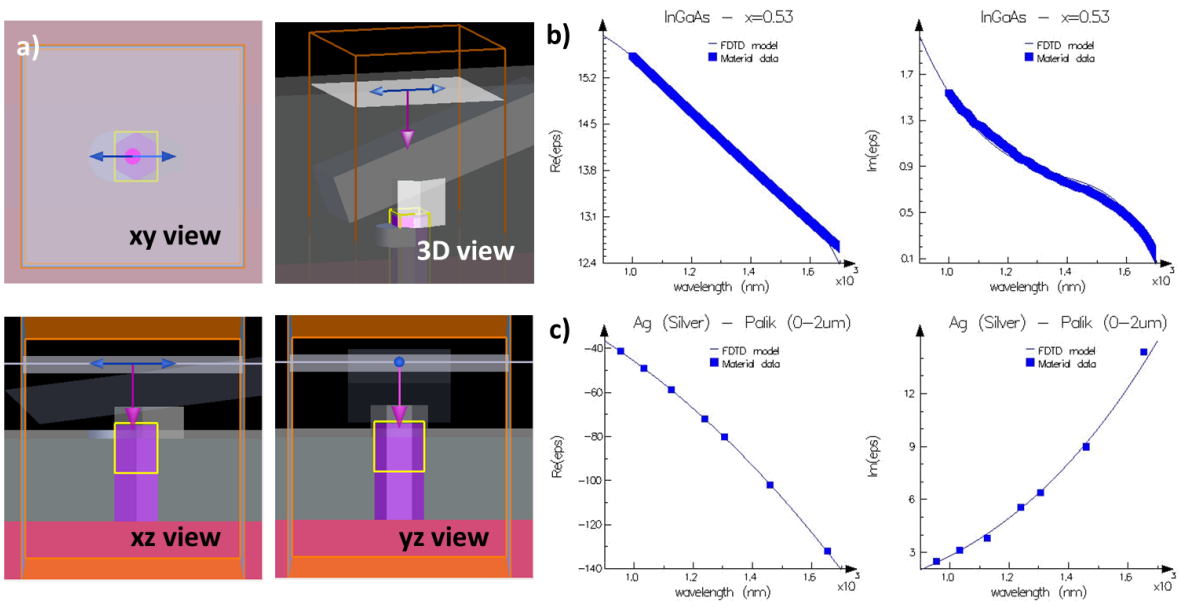

Figure 2 a) Simulation schematics at different viewpoints showing the simulation region, illuminating source, device structure, and the monitor used to record electric field. **b-c)** Permittivity values for **b)** $In_{0.53}Ga_{0.47}As$ and **c)** silver used in the simulation.

boundary condition that allow radiation to propagate out of computational area without interfering with the fields inside. For SPP simulation (section 2.3), the region size depends on the pitch at interest, and the boundary condition is set as periodic on both axes. Mesh is condensed around the region of the exposed nanowire. Depending on the size of the nanowire, the mesh step is between 5 to 15 nm per computation node.

(ii) The illuminating source is a normal incident plane wave source, with wavelength ranging from 900 to 1700 nm. The polarization is chosen as along the aperture instead of unpolarized to conserve simulation time. In principle, the same design procedure shown in this work can be repeated for any polarization of light.

(iii) The hexagonal $In_{0.53}Ga_{0.47}As$ nanowire absorber is modeled using the material property shown in Fig. 2b. To support LSP and SPP modes, silver is used due to its superior

performance in exciting surface plasmons [30,31]. A comparison in the quality factors for exciting surface plasmons between silver and other metals can be found in Appendix A. The optical property of silver used in the simulation is shown in Fig. 2c. From the SEM image in Fig. 1b, the metal cap on top of the nanowire is slanted as a result of the angled metal deposition. The effect is modeled by artificially etching the metal cap with a slanted angle as shown in the xz view in Fig. 2a. The etch on the metal cap will remain to be included in all simulations, even though the outline of such etching will be absent for the rest of the schematics shown in this work to avoid complicated figures. The geometry of the metal cap and the nano aperture will be scaled accordingly when the diameter or the exposed height of the nanowire is changed.

(iv) Electric field data recorded by a monitor can be used to calculate the QE or to show the electric field profile of a structure. Evaluation of QE is based on the following equation:

$$QE(\omega) = \frac{\frac{1}{2}\int_V \omega |E(\omega,x,y,z)|^2 \, \varepsilon''_{nw}(\omega) \, dV}{Source\ Power} \qquad (1)$$

where ω is the frequency, $E(\omega,x,y,z)$ is the electric field intensity, and $\varepsilon''_{nw}(\omega)$ is the imaginary part of the nanowire permittivity. In Lumerical, monitors can only be defined as parallel to x-, y-, or z- axis. Therefore, a 3D monitor cube is used to record the electric field inside the nanowire absorber. To conserve computation memory, only the top half of the nanowire is monitored, as the electric field of the bottom half of the nanowire is negligible. Since the nanowire is hexagon in shape, the monitor cube will record unnecessary electric field information outside the nanowire. To overcome this issue, the recorded electric field data points are passed through a filter that determines whether a

point is located inside the nanowire by testing the material index of that point. The filtered electric field is then integrated over the volume of the nanowire inside the monitor, which is then normalized by the source power, or the amount of power injected into the simulation,

$$Source\ Power(\omega) = \frac{1}{2}\int_S real\left(P_{source}(\omega)\right)\ dS \qquad (2)$$

where $P_{source}(\omega)$ is the Poynting vector of the source, and S is the size of the source. The code for calculating QE using monitors in Lumerical is shown in Appendix C.

2.2 Localized surface plasmon optimization

The two main parameters that can affect the LSP resonance are the wire diameter (*wd*) and the exposed height (*xh*) as shown in Fig. 1c. Wire diameter is defined as the flat-to-flat distance of the wire, as it gives more accurate measurements compared to corner-to-corner distance measurements in SEM images. To pinpoint the best geometry for the detector, both parameter sweeps are modeled. Note that eq. 1 can no longer be used for the evaluation of power absorbed in a PML simulation. Instead, the formula has to be modified to account for the correct distribution of the incident power (Appendix C). The figure-of-merit, absorption cross-section, is calculated as below:

$$Absorption\ cross\ section(\omega) = \frac{\frac{1}{2}\int_V \omega |E(\omega,x,y,z)|^2\ \varepsilon''_{nw}(\omega)\ dV}{source\ intensity} \qquad (3)$$

where the normalization factor is source intensity instead of source power.

2.2.1 Nanowire diameter

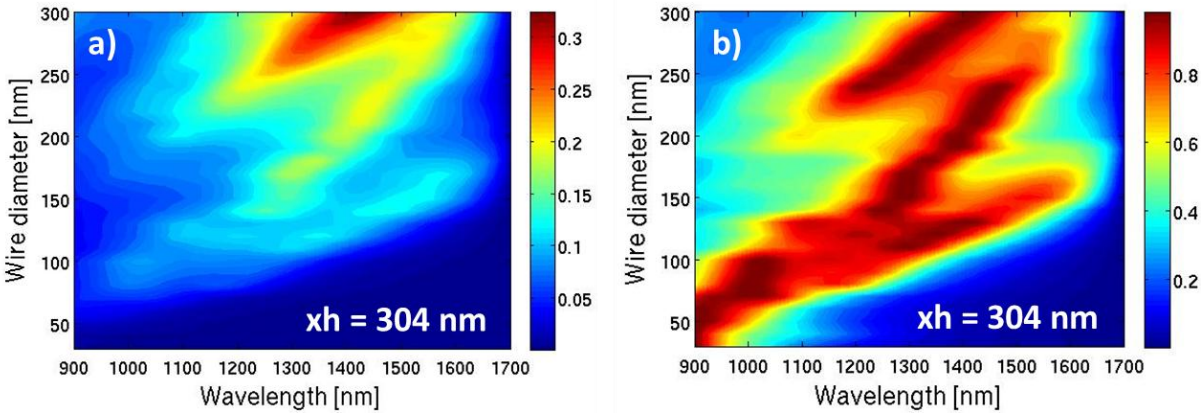

Figure 3 a) The absorption cross-section on different wire diameters (*wd*) in a PML simulation is plotted. The exposed height (*xh*) is kept at 304 nm. **b)** Each spectrum is normalized by the maximum absorption cross-section to show selectivity of the spectra.

The optimization of the 1250 nm detector will be demonstrated in detail here. Shown in Fig. 3a is the result of *wd* variation in a PML calculation. Exposed height is fixed at 304 nm, while the width of the hole is linearly scaled as the *wd* is varied. In bottom-up MOCVD nanowire growth, *wd* = 300 nm is approaching the upper limit, further increase in width will result in nanowire arrays with small aspect ratio. In general, larger *wd* gives higher absorption cross-section, which might not be at all surprising since more material is available for absorbing the incident light.

While a high absorption cross-section peak is favorable in getting a better photoresponse, the selectivity of the absorption peak is equally important. For example, if *wd* = 300 nm is chosen to build a 1550 nm detector solely based on its high absorption cross-section, the result will be detrimental since most of the photoresponse will instead be contributed from the 1400 nm peak. To have a better understanding of the selectivity, each spectrum in the contour plot is normalized by its maximum absorption cross-section as shown in Fig. 3b. Considering both

absorption cross-section and selectivity, there are two candidates for the 1250 nm detector: *wd* = 140 and 250 nm. While both of them are not perfect in terms of selectivity and sustain a secondary mode at a longer wavelength, *wd* = 250 nm is a better choice for the detector given that 1) it has a higher absorption cross-section which can provide higher photoresponse, and 2) it has the potential to suppress its secondary peak after an *xh* optimization.

The second reasoning can be realized by studying the electric field profiles for the two wire sizes in Fig. 4. For *wd* = 140 nm, the spectral peak at λ = 1250 nm shows a LSP mode

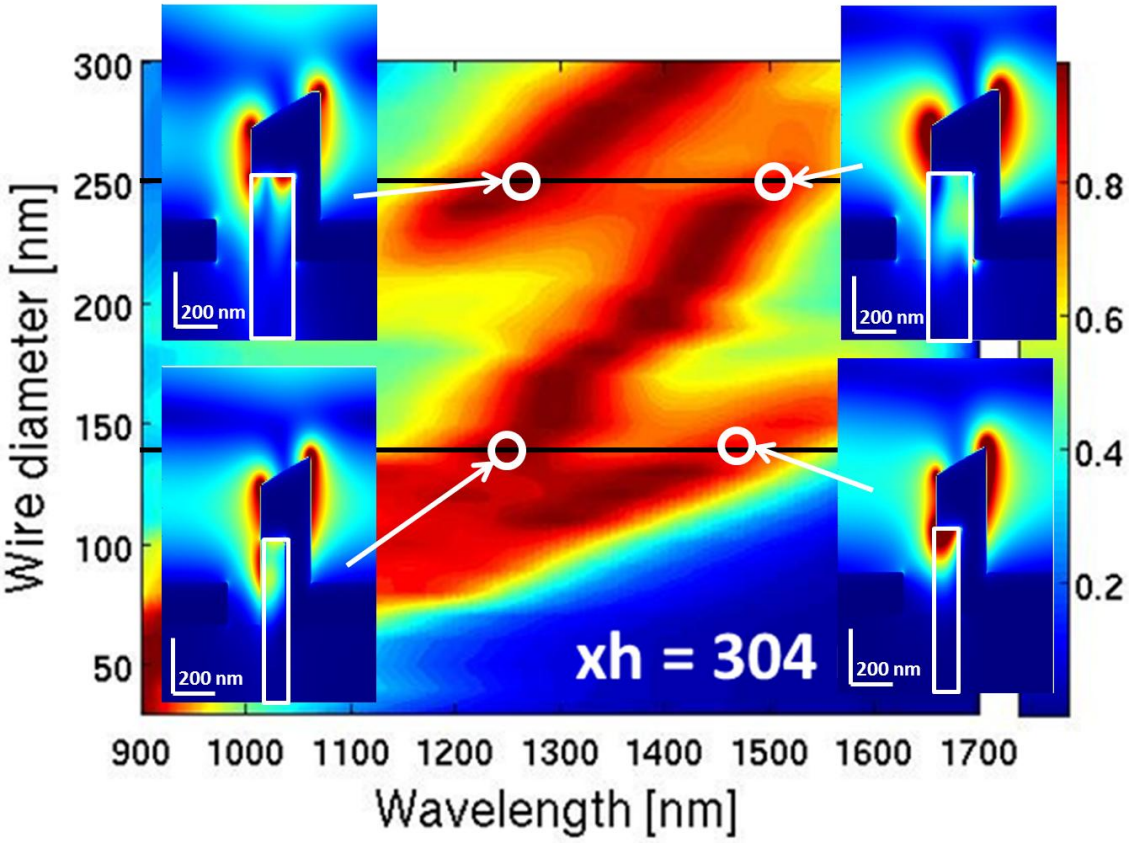

Figure 4 Comparison between *wd* = 140 and 250 nm. In both cases, two different types of modes can be observed: one excited closer to the center of the exposed tip (*wd* = 140 nm, λ = 1250nm; *wd* = 250 nm, λ = 1500 nm); and one near the metal-cap/nanowire interface (*wd*=250 nm, λ = 1250 nm; *wd* = 140 nm, λ = 1475 nm). Due to the nature of the modes, the former type varies in strength given a change in *xh* while the latter type is independent of *xh*. Therefore, by changing *xh*, one mode can be suppressed while the other remains unaffected.

spreads out at the center of the exposed tip, while the spectral peak at λ = 1475 nm shows a mode closer to the metal-cap/nanowire interface. For *wd* = 250 nm, an opposite case is shown, where the lower wavelength peak (1250 nm) has an interface mode, while the higher wavelength peak (1500 nm) has a exposed center mode. The significance of identifying the location of the modes is to determine if there are any *xh* dependencies in any of them. Intuitively, the exposed center mode will most likely be affected by any variation in *xh*, while the interface mode will not.

This suggests that to improve the selectivity for a 250 nm diameter wire, *xh* can be decreased to reduce the optical absorption at λ = 1475 nm while keeping the variation in the 1250 nm peak minimal. On the other hand, for the case of *wd* = 140 nm, a seemingly well argument would be to say that by increasing *xh*, the optical absorption at λ = 1250 nm can be increased, thus achieving a better selectivity. However, the fact that this mode is depended on *xh* means that as *xh* is varied, the resonant wavelength will also be affected. Therefore, while it is possible to obtain a better selectivity spectrum on the *wd* = 140 nm structure by varying the *xh*, the resonant wavelength will no longer remain at λ = 1250 nm. To conclude, the *wd* = 250 nm wire will be chosen and will serve as the starting point for an optimized 1250 nm detector.

2.2.2 Nanowire exposed height

Obviously, the next step then is to reduce the *xh* for the *wd* = 250 nm wire in order to suppress the secondary peak. The range of *xh* studied here is in between 204 and 504 nm. Given that the metal thickness is approximately 150 nm, the lower limit of 204 nm is chosen to have a large enough “opening” of the nanowire tip for sufficient light to be brought in to the nanowire. The upper limit of 504 nm on the other hand, is set based on practical fabrication consideration that the metal coating along the sidewall of the wire has to be continuous for electrical contact.

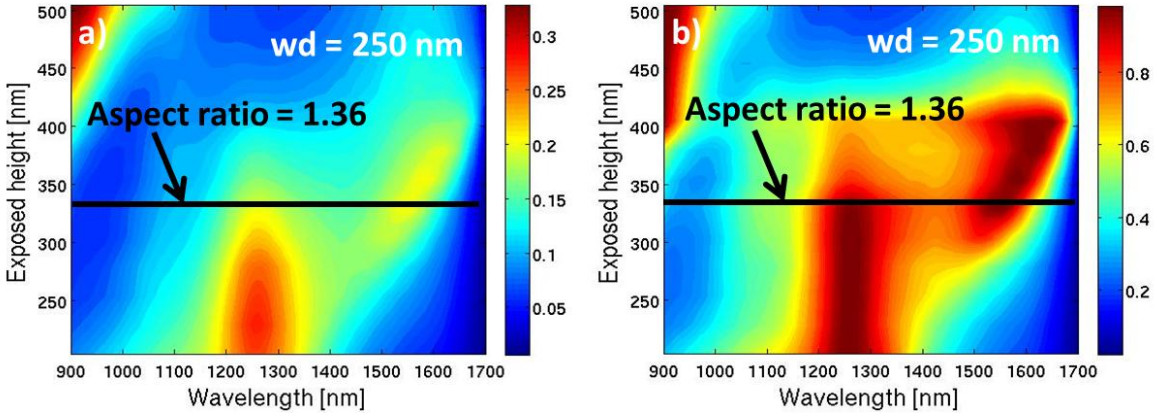

Figure 5 a) Exposed height variation in a PML simulation with *wd* = 250 nm. **b)** Each spectrum is normalized by the maximum absorption cross-section to show the selectivity of the spectra. The λ = 1250 nm mode (metal-cap/nanowire interface mode) shows no wavelength dependency on the *xh*; whereas the λ = 1500 nm mode (excitation mode at the center of the exposed tip) becomes prominent only when sufficient *xh* "opening" is provided to the structure, or simply when the aspect ratio is above 1.36.

Figure 5 shows the *xh* variation for the *wd* = 250 nm nanowire. Agreeing with the conclusion drawn from the above section, as the *xh* is lowered, the exposed tip center LSP mode is no longer confined, leaving only the *xh* independent interface mode excited at λ = 1250 nm.

To simplify the difficulty in tracking both *wd* and *xh* at the same time, the two parameters can be combined into one variable defined as the aspect ratio (*xh*/*wd*). In the case for *wd* = 250 nm, *xh* = 340 nm is approximately the borderline that separates between the two different kind of modes. In other words, an aspect ratio < 1.36 (340/250) favors the interface mode, whereas an aspect ratio > 1.36 favors the exposed tip center mode. Judging from the contour plot, the optimized geometry for the nanowire is *wd* = 250 nm and *xh* = 229 nm (aspect ratio ≈ 0.9) for a 1250 nm detector.

Moving on to the design of the nanowire for the 1050 nm detector, the *xh* = 304 nm contour plot in Fig. 3 can again be the starting point. The only available spectral peak is with the

wd = 80 nm structure. It is however, a poor candidate because of the limited photoresponse due to the low *wd* and the poor selectivity due to the broad spectral peak. It will therefore be a great asset if the concept derived in the previous section can be used to uncover a better geometry with a different *xh*. One possible direction is to extend the metal-cap/nanowire interface mode in the *wd* = 250 nm structure to a lower wavelength as shown in Fig. 6a.

Judging from the metal-cap/nanowire interface mode extension in the *wd* = 250 nm structure, the mode will have an excitation wavelength of 1050 nm if the *wd* is approximately 200 nm. The same aspect ratio of 1.36 calculated from before will be used as the upper bound for

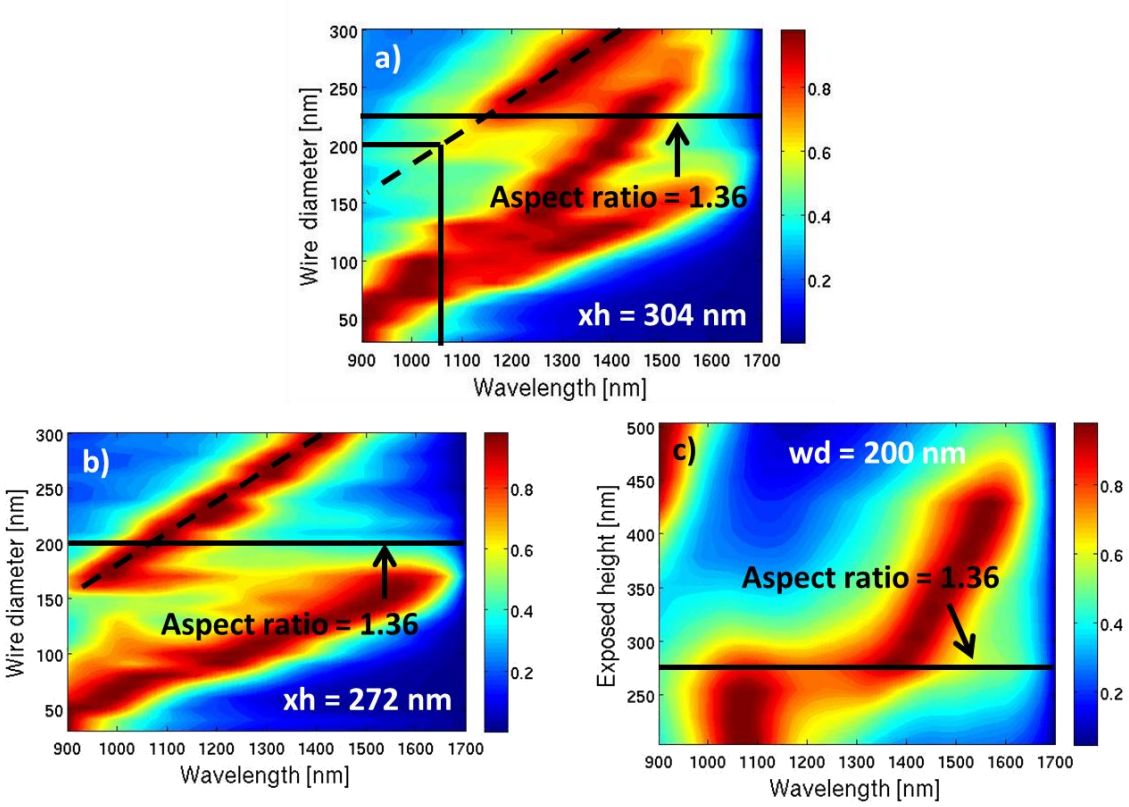

Figure 6 a) Normalized contour plot for *xh* = 304 nm. Dashed line showing the interface mode extending to *wd* = 200 nm for a λ = 1050 nm resonance. **b)** Normalized contour plot for *xh* = 272 nm. Extension of the interface mode to *wd* = 200 nm by using an *xh* of (200 nm × 1.36) = 272 nm. **c)** Normalized contour plot for *wd* = 200 nm. As predicted, the aspect ratio = 1.36 line can be seen as the borderline in favoring one mode versus the other.

the structure to sustain the favorable interface mode. Based on the information, an *xh* of (200 nm × 1.36) = 272 nm will be the initial guess for the interface mode to appear at 1050 nm. Figure 6b shows the *wd* contour plot for *xh* = 272 nm. As shown in the plot, the interface mode is extended to *wd* = 200 nm for a 1050 nm excitation. In Fig. 6c, the *xh* contour plot is shown, and as predicted, the separation between the two modes lies approximately at *xh* = 272 nm. For the optimization for *xh*, 204 nm will be chosen for its highest absorption cross-section for the interface mode. The nanowire geometry for the 1050 nm detector therefore, is settled as *wd* = 200 nm and *xh* = 204 nm.

For a 1550 nm detector, the mode that is used in both 1050 and 1250 nm detectors is not longer available since the mode stops at λ = 1450 nm at the maximum 300 nm *wd* (Fig. 3). Fortunately, for both *xh* contour plots in Fig. 5b and 6c, the secondary mode is located near the 1550 nm region. A 1550 nm detector can be achieved simply by extending the *xh* of the *wd* = 200 nm structure. The chosen geometry for the 1550 nm detector is *wd* = 200 nm and *xh* = 379 nm. A summary on the three optimized wires is shown in Table 1.

Table 1 Nanowire geometry for each detector

	Wire diameter, *wd* [nm]	Exposed height, *xh* [nm]
1050 nm detector	200	204
1250 nm detector	250	229
1550 nm detector	200	379

To illustrate the concept of building a hyperspectral detector from the three LSP-optimized nanowires, Fig. 7a shows a structure schematic by simply putting them together and utilizing LSP as an absorption enhancement mechanism. As simple as the arrangement seems, the design can already be considered as a pixel for the camera. Control on the different positions and diameters of the nanowires can be achieved by lithographical control over the patterned holes on the SiO_2 mask before the MOCVD growth, while the *xh*'s of the nanowires can be obtained by a series of subsequent selective-area etching on the nanowires (Appendix B). The proposed structure is simulated, with distance between each detector to be 1414 nm. The

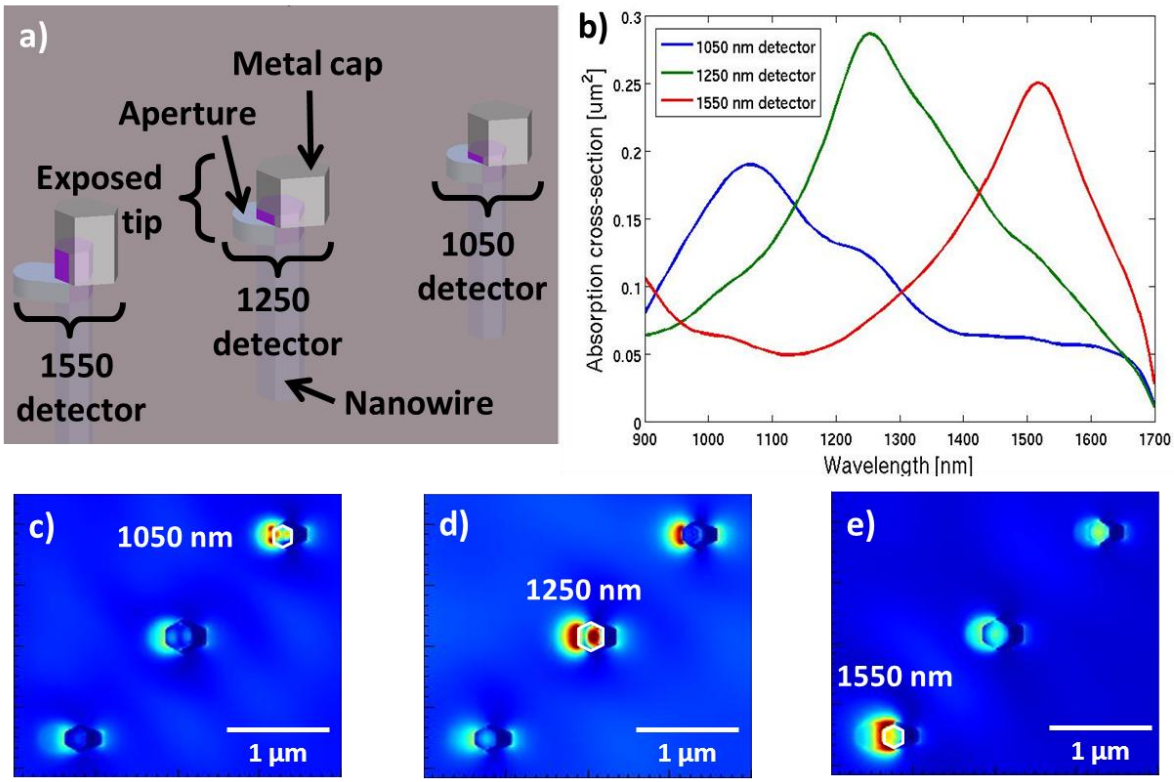

Figure 7 a) Schematic of the LSP-optimized hyperspectral pixel. **b)** Absorption cross-section of the three detectors showing reasonable absorption strength at their responsible resonant wavelength. **c-e)** Top down electric field profiles for the three detectors at **c)** 1050, **d)** 1250, and **e)** 1550 nm excitation wavelength.

absorption spectra and the electric field profiles of the structure are shown in Fig. 7b-e. The results are encouraging, suggesting sufficient selectivity at all three wavelengths. This preliminary structure design will serve as the basis for the forthcoming design of the SWIR hyperspectral detector.

2.3 Surface plasmon polariton

Although the above LSP-optimized design will fulfill the basic functionality of a hyperspectral detector, to claim it as a high performance detector design is hardly convincing unless there is some notable improvement on the selectivity of each peak. The fact that a camera is often arranged in periodic pixels suggests that periodic metal gratings can be designed for additional SPP mode coupling with the optimized LSP, resulting in a hybridized mode. The SPP resonance due to periodic arrangement is:

$$\lambda_{max} = \frac{P}{\sqrt{i^2 + j^2}} \sqrt{\frac{\varepsilon_M \varepsilon_D}{\varepsilon_M + \varepsilon_D}} \qquad (4)$$

where P is the pitch, $\varepsilon_M, \varepsilon_D$ are the permittivities of the metal and dielectric respectively, i, j correspond to the different SP modes in a square array. This equation describes the first order approximation on the conservation of momentum condition necessary to couple normally incident radiation to propagating SPP modes on a metal/dielectric interface. The dependency of a SPP resonance lies on the "macroscopic properties" such as the lattice pitch and the metal permittivity, and never takes into account the "microscopic structure" within a lattice cell.

Using the equation, theoretical SPP resonances can be calculated. Three types of metal/dielectric interface will be considered: silver/air, silver/bcb, silver/InGaAs. For each type of SPP mode, only the zero-order resonance will be included (i = 1) since higher order modes are located outside the 900 – 1700 nm range. Figure 8 solid lines show the pitch dependencies on the SPP modes (Appendix E). This plot provides a basic guideline in choosing a pitch size that suits best in obtaining a certain SPP mode. While the equation provides predictions on the resonant positions and suggests the origin of each of the SPP resonance, it does not give any information on how well the structure supports each of them. Simulation on periodic arrays will

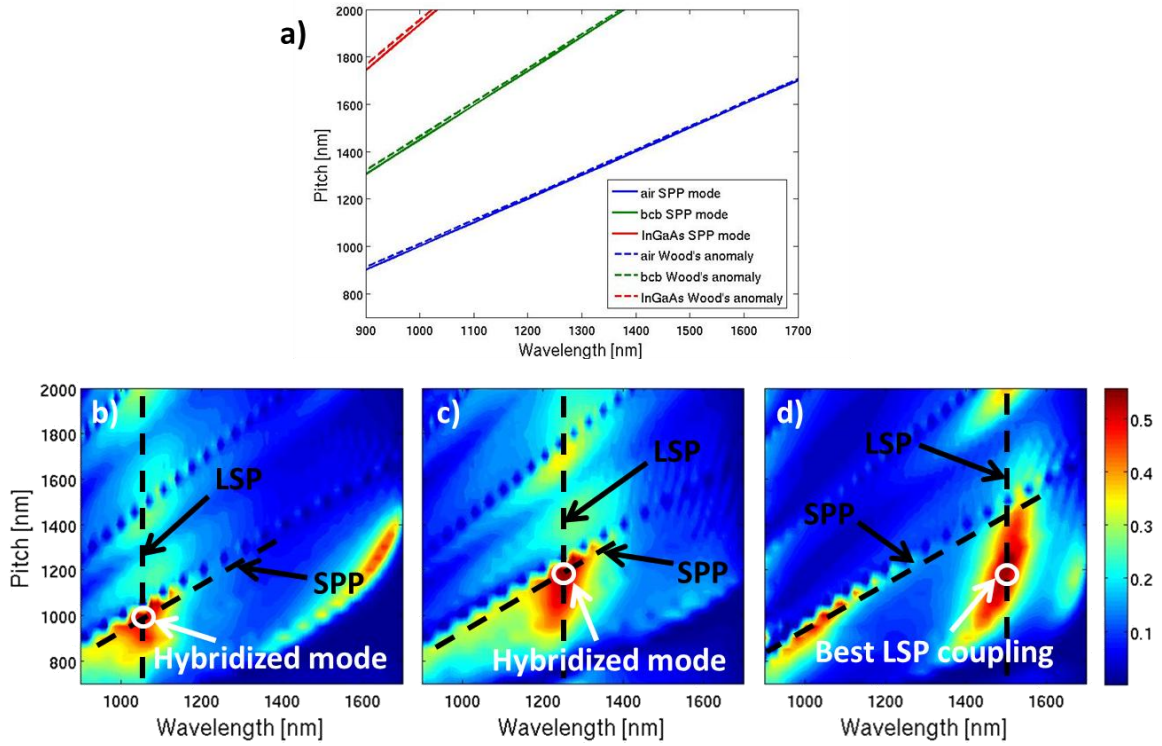

Figure 8 a) Theoretical calculations on the SPP modes and the Wood's anomalies for the silver/air, silver/bcb, and silver/InGaAs interface. **b-d)** Pitch dependence on the QE of the periodic detectors optimized for the absorption of **b)** 1050, **c)** 1250, **d)** 1550 nm. The three zero absorption lines on each plot are caused by the Wood's anomaly. LSP excitations can be seen as the vertical high absorption region in all three cases, with the pitch-independency effect especially profound at lower wavelengths. Hybridized modes are formed when SPP mode couples with a vertical LSP band.

be done to both confirm the validity of the equation in the proposed structure and also to evaluate the coupling strength of the SPP modes into the available LSP modes.

The periodic array simulation is modeled by setting the boundary condition to periodic boundaries in both x- and y- directions. Incident plane wave source is used, and power absorbed (or QE) is calculated using eq. 1. The variations on pitch for all three LSP-optimized nanowires are shown in Fig. 8b-d. Before discussing the SPP resonant peaks in the contour plots, the three zero absorption lines shown in all three plots will be addressed first. (The discontinuity of the line is caused by the sparseness of the available data points.)

Ebbesen et al. have extensively investigated this phenomena, reporting a highly unusual transmission properties of metal film perforated with a periodic array of subwavelength holes [32]. They have observed that the zero-order transmission spectra exhibit well-defined maxima and minima of which the positions are determined by the geometry of the hole array. The minima are identified to be caused by Wood's anomaly [33], which occurs when a diffracted beam becomes tangent to the plane of the grating, and that the maxima are the results of a resonant excitation of SPP. The equation that formulates the Wood's anomaly is as follows:

$$\lambda_{max} = \frac{P}{\sqrt{i^2 + j^2}} \sqrt{\varepsilon_D} \qquad (5)$$

Compared to eq. 3, the Wood's anomaly differs in the latter term, where only the dielectric permittivity is considered. If the Wood's anomaly is to be calculated, the minima will be found slightly blue-shifted from the position of the SPP maxima (Fig. 8 dashed lines). While it is pointed out in previous sections that SPPs are involved in the exceptional transmission properties

of the lattice array, a more detailed analysis indicates that the spectra are actually determined by the superposition of both phenomena, namely, the Wood's anomaly and the SPP resonance [32].

With the established understanding on both phenomena, it can then be concluded that the sharp contrast in the absorption spectra is due to the Wood's anomaly providing the minima and the SPP resonance contributing to the maxima. This results in reduced full-width-half-maximum (FWHM) for the absorption peaks, and can be leveraged in the designing of the hyperspectral camera to achieve better selectivity. Based on Fig. 8b-d, the best SPP coupling mode is the zero-order silver/air mode in all three nanowire detectors.

The effect of LSP can be shown in Fig. 8b-d as a vertically high absorption band, and the SPP-LSP hybrid mode can be found when the SPP mode intercepts with the LSP mode. For the 1050 and 1250 nm detectors, the hybridized modes provide the highest absorption for the structure as shown in Fig. 8b and c; for Fig. 8d however, the hybridized mode is no longer beneficial. This is due to the LSP mode no longer preserving the "pitch independency" property at longer wavelengths. In other words, if the distance between two nanowire absorbers is considered to be close enough that one nanowire can affect the excitation of LSP of another, the LSP resonance will no longer be entirely pitch independent. This effect is especially profound in longer wavelengths as shown in Fig. 8d, where the vertical LSP absorption band is less uniform compared to Fig. 8b and c. As a result, there exists an optimal pitch for the LSP resonance for the 1550 nm detector that gives higher QE than the hybrid mode. Fig. 9 and Table 2 show the spectra and the geometries of the three periodic detector arrays.

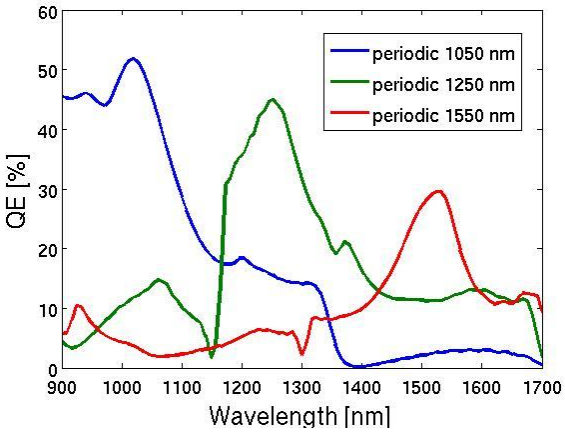

Figure 9 QE for the three detector arrays. Note that each spectrum corresponds to a periodic FPA of nanowires optimized for one wavelength absorption, and therefore does not represent the QE of a hyperspectral camera.

Table 2 Nanowire geometry for each detector

	Wire diameter, *wd* [nm]	Exposed height, *xh* [nm]	Pitch, P [nm]
1050 nm detector	200	204	800
1250 nm detector	250	229	1150
1550 nm detector	200	379	1300

2.4 Pixel design

Perfect as the spectra may seem, it is both difficult in reality to overlay three nanowire arrays with different pitch sizes given the limited space on the pixel. Several nanowires throughout the surface of the pixel will end up lying on top of each other, and more of them will get close enough to others that render the previous LSP optimization scheme useless. Therefore, instead of implementing two dimensional periodic array structures, an array structure periodic

only in one-dimensional will serve as the solution to the spatial discrepancy among the nanowires.

The arrangement of the camera pixel will be organized into rows (or columns) of nanowire detectors, where each row (column) consists of one type of detector specified to absorption a particular wavelength. The horizontal (vertical) inter-wire spacing of the detectors is the optimized pitch size in the previous section, while the vertical (horizontal) spacing will be chosen as 1000 nm. The next question then is which axis should be chosen as periodic alignment. Theoretically, SPP mode coupling does not differ in one direction versus the other as long as the pitch is kept constant (eq. 3). However, since the proposed structure is not entirely symmetric, it should not come as a surprise if the SPP mode actually couples better one way or the other.

To better understand the SPP coupling on each axis, PML simulations are done on the 1250 nm detector where the nanowires are aligned 1) vertically, 2) horizontally, 3) both vertically and horizontally, and 4) stand alone (no periodicity on either axes) (schematics in Fig.

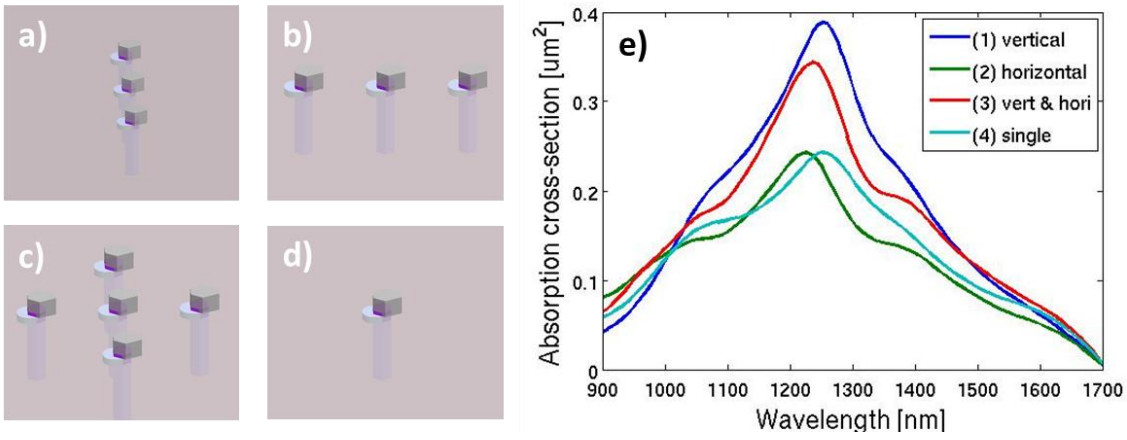

Figure 10 a-d) Schematics for the 4 types of alignment based on the 1250 nm detectors. **e)** The absorption cross-section spectra for each case. Vertical alignment (1) has the highest absorption cross-section, while horizontal alignment (2) has no absorption enhancement and has the same magnitude as a single nanowire (4).

10a-d). For all periodic alignment in this set of simulations, only the nearest neighbor will be taken into account, since the structure is utilizing at most the zero-order mode. Shown in Fig. 10e are the spectra for the four cases. Contrary to intuition, periodic on both axes (3) does not yield the best absorption, but instead, the best case belongs to the vertical alignment configuration (1). The horizontal alignment (2) on the other hand, hardly contributes to any increase in absorption, and has the same absorption cross-section as a single nanowire (4).

The final design schematic of the hyperspectral camera pixel is shown in Fig. 11a. A 6 µm × 6 µm pixel is simulated, with 6 columns of detectors. Each column contains one type of vertically aligned detectors with the optimized pitch found in Table 2. For the 1050 nm detectors, 7 devices are aligned in each column, giving a total number of 14 nanowire devices per pixel. For the 1250 and 1550 nm detectors, a total of (2×5) = 10 devices exist on each pixel. Ideally, the QE of one type of detector should be evaluated by summing each individual nanowire QE in

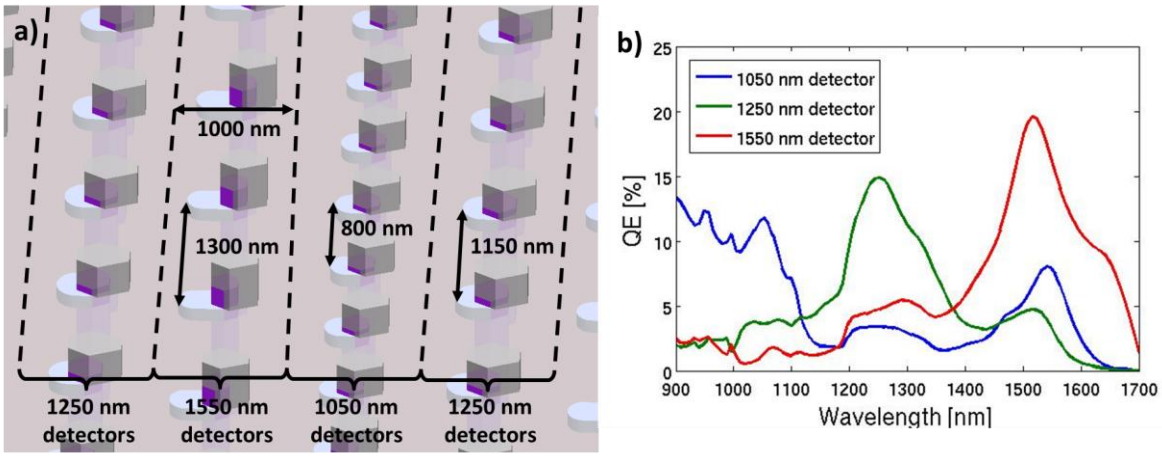

Figure 11 a) Final design schematic of the hyperspectral camera pixel. The detectors are vertically aligned with the optimized pitch for the best absorption enhancement. Each pixel is 6 µm × 6 µm, with 6 columns of detectors, giving a total of 14× 1050 nm nanowire detectors, and 10× 1250 and 1550 nm detectors per pixel. **b)** The QE spectra for the three detectors are shown. Unlike Fig. 8, these QE spectra represent the performance of the nanowire detectors when put into a pixel of a hyperspectral camera.

a pixel, as the QE of each nanowire device will vary slightly depending on the location of them within a pixel. This however, will require tremendous computation power and memory. Therefore, an approximation has to be made; and the QE for one type of detector is estimated by multiplying the number of devices in the pixel with the QE of a nanowire device located near the center of the pixel. The QE spectra for all three detector types are shown in Fig. 11b. The QE is significantly lower than the one shown in Fig. 9, indicating a weaker coupling mode in the devices when fitting into a pixel. This reduction is mostly contributed by a degradation in the SPP coupling of the device, as the 1050 and 1250 nm detectors suffer most from putting them into a pixel.

3 Summary

This work has presented an optimization procedure on the design of a SWIR hyperspectral camera. The design uses nanowire array as a mean to reduce dark current while increasing the surface area for enhanced optical collection. The surface of the nanowire array is deposited with silver at an angle to sustain metal/dielectric surface plasmon modes. Two types of surface plasmon modes are utilized: LSP and SPP. The LSP mode is optimized by changing the geometry of the nanowires, while the SPP mode is optimized by changing the pitch of the array. Several types of periodic alignment schemes are suggested, and the vertical alignment configuration is chosen for the best optical absorption. The resulting hyperspectral camera will be sensitive at 1050, 1250, and 1550 nm with QE of 12%, 15%, and 20% respectively, assuming ideal conversion between optical photoabsorption and electrical photocurrent.

Compared to state-of-art works, the proposed design eliminates the need for a filter, in which the metal gratings on the nanowire array act as a filter to sort photons. Another astounding achievement of the design is the significant reduction on the pixel size of the camera. The smallest pixel size in current commercialized SWIR cameras featuring small size, weight, and power (SWaP) imagery is 12.5 µm [2,34–36], while the pixel size in this work suggests only 6 µm, promising a > 50% size reduction. The tremendous reduction in size is attributed to the use of surface plasmons, which unlike conventional light focusing mechanisms, is not limited by the diffraction limited spot size of light, and can significantly reduce the pixel size of the camera as shown in this work. The tradeoff however, is the moderate QE and sensitivity of the detectors when they are compactly packed onto the limited space on the pixel.

Perhaps the most interesting future work is to further optimize the pixel design. For example, the lateral distance between the columns of detectors could be an important parameter to be optimized. This affects the pixel in two ways: 1) it directly controls the lateral size of the pixel, and 2) it affects the "color cross-talks" between detectors, an effect that is especially strong on the 1050 nm detector as shown in Fig. 11b with significant absorption at $\lambda = 1550$ nm. With better optimization on the pixel design, the QE is expected to increase, resulting in improved performance on the camera.

Appendix A – Surface plasmon resonances

A brief discussion of surface plasmon will be presented here to gain some insights and directions on the design. In the simplest term, surface plasmon is a quantum of electron density oscillation on a metal surface. When an incident electromagnetic (EM) wave enters an interface with high permittivity difference, which usually occurs on a metal/dielectric interface, there exists a critical angle for the incident wave to be trapped at the interface. These EM wave loses energy by transferring momentum to the surface electrons on the metal. As these surface electrons get excited, they start to form energized electron density packets that travel as a wave on the metal surface. Given the right condition and geometry, these surface electron density waves can resonate, giving raise to surface plasmon resonances.

Surface plasmon resonances can be classified into two types: propagating surface plasmon resonance (SPP) and localized surface plasmon resonance (LSP). Both of which can lead to an enhancement in EM field at the metal surface, thus resulting in extraordinary sensitivity to the metal surface conditions, which is widely utilized in optical, chemical, and biological surface sensing. The behavior of SPP and LSP is fundamentally different, and can be derived from the Maxwell's equations with associated metal/dielectric boundary conditions. For SPP, the boundary conditions are set so that 1) light propagates from one medium to another with high permittivity change (ex. air to metal), and 2) the EM field of the wave decays exponentially with increasing distance away from the interface. The explicit solution from the Maxwell's equations for such wave is

$$k_{sp} = \frac{\omega}{c}\left[\frac{\varepsilon_D \cdot \varepsilon_M(\omega)}{\varepsilon_D + \varepsilon_M(\omega)}\right]^{1/2}$$

where ε_D and ε_M refers to the permittivity of metal and dielectric respectively (ε_M is frequency dependent due to the dispersive behavior of metal).

In contrast, LSP is a localized EM field existing in subwavelength and bounded geometries. The dispersion relation of an LSP can be derived using the Maxwell's equation together with the Laplace's equation describing the geometry. By setting the electrostatic potential (ϕ)of a nanostructure (ex. a sphere) to be finite within the structure and vanishes at infinity outside the structure, and with boundary conditions ensuring the continuity of ϕ and $\frac{\partial \phi}{\partial r}$, the dispersion relation of an LSP can be obtained. For a small sphere, the solution is

$$\omega_{lsp} = \omega_p \left[\frac{1}{2\varepsilon_0 + 1} \right]^{1/2}$$

where ω_p is the frequency of bulk longitudinal electron excitations, or the plasma frequency.

It can be realized from the relation that LSP is characterized by discrete frequency, independent of wavenumber k, which give rise to the non-propagating property of an LSP.

To quantify the performance of a metal in exciting the two types of surface plasmons, quality factors for LSP and SPP for a specific type of metal can be calculated. The formulation is as follows [30]:

$$Q_{LSP} = \frac{-\varepsilon'(\omega)}{\varepsilon''(\omega)}, \quad \text{assuming a spherical metal nanoparticle in the LSP case.}$$

$$Q_{SPP} = \frac{\varepsilon_m'(\omega)^2}{\varepsilon_m''(\omega)}.$$

The table below shows the quality factors for various types of possible low-loss plasmonic candidate materials. Clearly, silver serves as a good candidate for both LSP and SPP resonances.

Table Summary of the quality factors of a number of possible low-loss plasmonic candidate materials. The maximum value of the quality factor (up to 2.5 μm) and the wavelength at which the maximum occurs are tabulated for each material and each of the four applications. The quality factors at 1.5 μm (for nanophotonic applications) are also presented. Quality factors for TO devices were calculated at the crossover frequency where $\varepsilon' = 0$.

Material	LSPR & SPR		SPP		TO Devices	Superlens	Comments
	Maximum Q_{LSPR} (λ)	Q_{LSPR} (1.5 μm)	Maximum Q_{SPP} (λ)	Q_{SPP} (1.5 μm)	Q_{TO} (λ)	Q_{S} (λ)	
Ag*	392 (1.08 μm)	39.3	23413 (1.08 μm)	4530	1.82 (326 nm)	0.3 (339 nm)	Good for LSPR & SPP
Au*	16.66 (0.89 μm)	10.63	1410 (1.94 μm)	1140	0.29 (207 nm)	−0.13 (252 nm)	Good for LSPR
Al	13.56 (0.113 μm)	5.55	2677 (2.5 μm)	1315	26.32 (82 nm)	0.52 (114 nm)	Good for LSPR in UV
Na*	37.8 (1.00 μm)	27.3	1889 (2.25 μm)	1179	NA***	0.48 (312 nm)	Difficult to process
K*	40.6 (1.17 μm)	19.2	1287 (2.25 μm)	419	22.22 (326 nm)	0.5 (438 nm)	Difficult to Process
KAu	1.3 (2.5 μm)	NA**	1.1 (2.5 μm)	NA**	1.72 (2.38 μm)	0.18 (2.52 μm)	Difficult to process
ITO*	2.72 (2.3 μm)	NA**	16 (2.3 μm)	NA**	1.54 (1.69 μm)	0.13 (1.88 μm)	Good for TO in NIR
AZO	3.28 (2.26 μm)	1.46	33.1 (2.5 μm)	2.33	2.16 (1.3 μm)	0.179 (1.46 μm)	Good for TO in NIR
GZO	1.8 (2.3 μm)	0.923	15.96 (2.5 μm)	1.01	1.22 (1.32 μm)	0.087 (1.48 μm)	Good for TO in NIR

* Ag and Au data ends at 2 μm, Na, K data ends at 2.25 μm, and ITO data ends at 2.3 μm.

** Crossover frequency for these materials corresponds with a wavelength above 1.5 μm. Thus, quality factors are not applicable for these materials at the telecommunication wavelength.

*** Crossover frequency data is not available.

Appendix B – Growth and fabrication

While the growth and fabrication of the devices are not the main focus of this project, a brief discussion will be brought here to show the practicality of the design. By careful control on the growth condition, both axial and coreshell [37–40] p-n junctions can be facilitated, offering intriguing possibilities promised by their confined junction area. For the device presented here, $In_{0.53}Ga_{0.47}As$ nanowires are grown using selective-area epitaxy on InP substrates by metalorganic chemical vapor deposition (MOCVD). The growth substrate is patterned with a SiO_2 mask (25 nm thick) using e-beam lithography and reactive-ion etching (RIE). The ability of lithographical control over the position and the diameter of the patterned holes enable the growth of periodic nanowire arrays with arbitrary wire diameter and height [41].

Following epitaxy, the nanowire array is planarized using benzocyclobutene (BCB), and etched back to expose the tip of the nanowires. The exposed height of the nanowire tips is another parameter that can be tuned by controlling the BCB etch time. Finally, the top metal contact is evaporated at 35° from the substrate normal to coat both top and the exposed side of each nanowire along with the entire surface interconnecting the wires. In this regard, the nanowire tip itself acts as a shadow mask that leaves the other side of the wire tip uncoated and forms a self-aligned nanohole adjacent to each nanowire. This metal nanohole array self-aligned to patterned nanowires eliminates the need for process-intensive lithography to separately define the subwavelength metal nanoholes [42].

To obtain nanowires with different diameters and heights, the following fabrication procedure can be used:

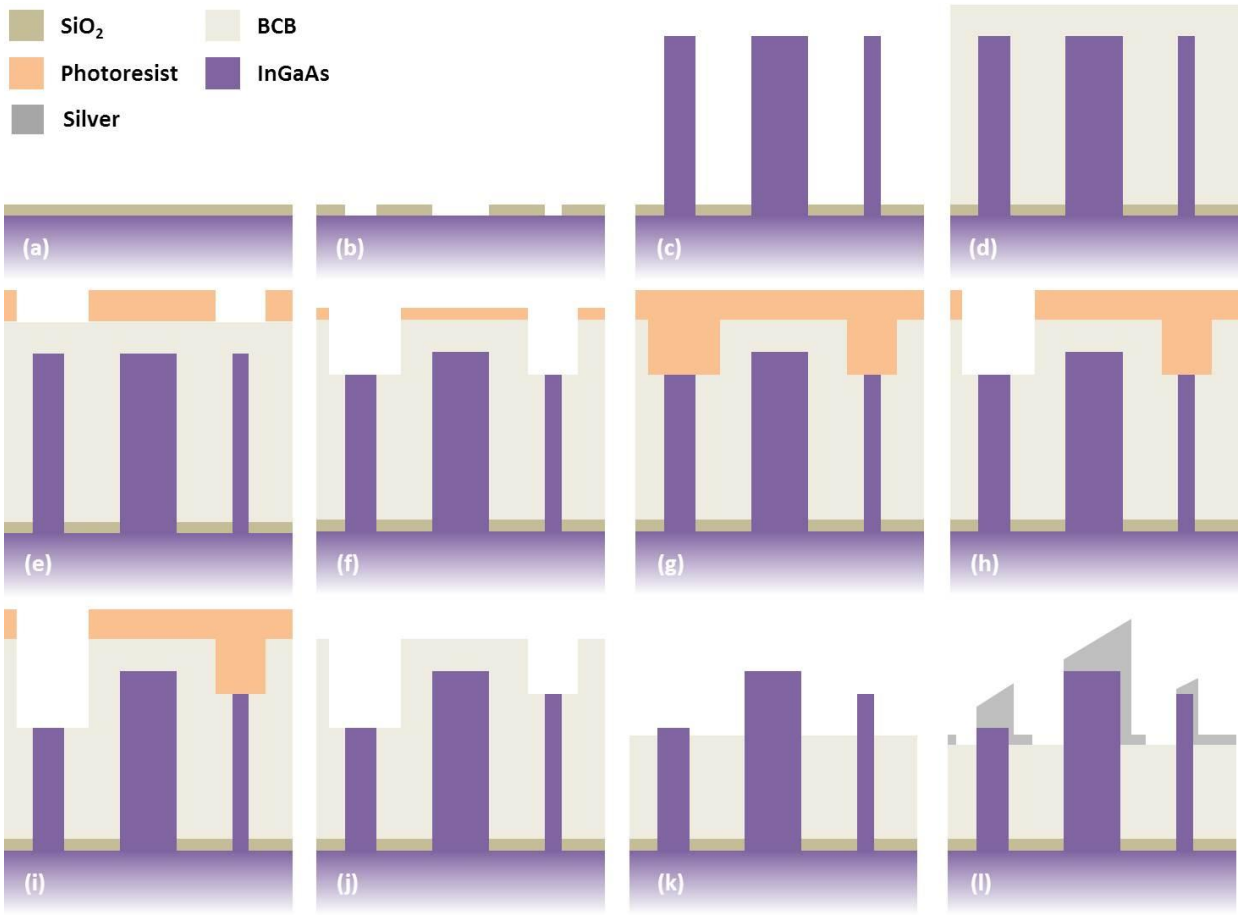

(a) SiO2 mask deposition

(b) Lithographic patterning

(c) MOCVD growth

(d) BCB coating

(e) Photoresist mask patterning

(f) Dry etching

(g) Photoresist mask patterning

(h) Dry etching

(i) Nanowire etching

(j) Photoresist removal

(k) BCB etch back

(l) Angled deposition

Appendix C – QE and absorption cross-section

$$QE(\omega) = \frac{\frac{1}{2}\int_V \omega |E(\omega,x,y,z)|^2 \, \varepsilon''_{nw}(\omega) \, dV}{source\ power}$$

$$Absorption\ cross\ section(\omega) = \frac{\frac{1}{2}\int_V \omega |E(\omega,x,y,z)|^2 \, \varepsilon''_{nw}(\omega) \; dV}{source\ intensity}$$

As shown in the equation, calculation of QE requires the knowledge of the incident source power, which is simply the source intensity times the size of the source. In a PML simulation however, the size of the source is undefined. If the size is chosen to be sufficiently large to represent the near-infinite size of the sensible light compared to the detector size, the QE will essentially drop to zero. On the other hand, if the size is too small, the source will fail to represent the absorption taken place in a FPA under illumination. For a meaningful QE calculation, the incident source has to be chosen not only as the exact size of the optical collection area, but also the exact shape of the collection area as well. Since the shape of the optical collection area is most likely to be non-rectangular, providing such incident source will be extremely difficult.

A more reasonable approach for a PML simulation is to use absorption cross-section as the figure-of-merit to determine the efficiency of optical absorption. The difference is simply the normalization factor: instead of normalizing to the source power (intensity times size), it normalizes to the source intensity of the incoming light. In physical terms, absorption cross-section is the measure of the ability to absorb light in a particular wavelength, with a unit of length squared. The source in a PML simulation for absorption cross-section calculation has to be large enough to ensure the detector is receiving all the light it is able to collect.

Appendix D – QE/absorption cross-section calculation in Lumerical

```
# Settings
getE2 = 0;  getPabs = 1;  getabsxs = 0;
pk = 1550;
moni_name = "profile";
index_name = "index";
struct_name = "";
pillar_name = "pillar";
#savename = "pk"+num2str(pk);
savename = filebasename(currentfilename);

# Initialize
 x = getdata(moni_name,"x");
 y = getdata(moni_name,"y");
 z = getdata(moni_name,"z");
 f = getdata(moni_name,"f");
 nx = length(x);
 ny = length(y);
 nz = length(z);
 nf = length(f);
 E = getelectric(moni_name);
 n = getdata(index_name,"index_x");

 ? "    Filtering...";
 temp_n = real(n(1:nx,1:ny,1:nz,1));
 pillar_x = getnamed(pillar_name, "x")+getnamed(struct_name,"x");
 pillar_y = getnamed(pillar_name, "y")+getnamed(struct_name,"y");
 pillar_z = getnamed(pillar_name, "z")+getnamed(struct_name,"z");
 index_x = find(x, pillar_x);
 index_y = find(y, pillar_y);
 index_z = find(z, pillar_z);
 pillar_n = temp_n(index_x, index_y, index_z, 1);

 fil_mat = matrix(nx,ny,nz);
 for(i=1; i<=(nx*ny*nz); i=i+1)
 {
  if(temp_n(i) == pillar_n)
    { fil_mat(i) = 1; }
 }
 full_filmat = matrix(nx,ny,nz,nf);
 for(j=1; j<=nf; j=j+1)
 {
  full_filmat(1:nx,1:ny,1:nz,j) = fil_mat;
 }
 E = E*full_filmat;

 eps = eps0*n^2;
 W = meshgrid4d(4,x,y,z,2*pi*f);

 if(getE2)
 {
  ? "    ... E2";
  E2_result = matrix(nf,2);

  ETot=integrate(E,1:3,x,y,z);
  E2_result(1:nf,1) = c/f*1e9;
  E2_result(1:nf,2) = ETot;
 }
 if(getPabs)
 {
  ? "    ... Pabs";
  Pabs_result = matrix(nf,2);

  SP = meshgrid4d(4,x,y,z,sourcepower(f));
  pabs = 0.5*W*E*imag(eps)/SP;
  pabsTot = integrate(pabs,1:3,x,y,z);
  Pabs_result(1:nf,1) = c/f*1e9;
  Pabs_result(1:nf,2) = pabsTot;
 }
 if(getabsxs)
 {
  ? "    ... absxs [um^2]";
  absxs_result = matrix(nf,2);

  SI = meshgrid4d(4,x,y,z,sourceintensity(f));
  absxs = 0.5*W*E*imag(eps)/SI;
  absxsTot = integrate(absxs,1:3,x,y,z)*1e6^2;
  absxs_result(1:nf,1) = c/f*1e9;
  absxs_result(1:nf,2) = absxsTot;
 }

? "Saving...";
savefile_header = " " + savename;

if(getE2)
{
 E2_savename = savename + ".E2";
 if(fileexists(E2_savename)) { rm(E2_savename); }
 write(E2_savename,savefile_header);
 write(E2_savename,num2str(E2_result));
}
if(getPabs)
{
 Pabs_savename = savename + ".pabs";
 if(fileexists(Pabs_savename))
{ rm(Pabs_savename); }
 write(Pabs_savename,savefile_header);
 write(Pabs_savename,num2str(Pabs_result));
}
if(getabsxs)
{
 absxs_savename = savename + ".absxs";
 if(fileexists(absxs_savename))
{ rm(absxs_savename); }
 write(absxs_savename,savefile_header);
 write(absxs_savename,num2str(absxs_result));
}

? "Done.";
? "";
```

Appendix E – MATLAB code for theoretical SPP calculation

```
function result = pitch_SPP()

 global plot_modes defined_mode_index;

 pitch = 700:50:2000;
         % SP:1,2,3,4
 plot_modes = [  1,0,0;  % air modes
              1,0,0;  % bcb modes
              1,0,0]; % user-defined modes
 defined_mode_index = sqrt(3.75);
            % SP1 -- SP 01, +/-10
            % SP2 -- SP 02, +/-11, +/-20
            % SP3 -- SP 03, +/-12, +/-21, +/-30
 result = zeros(length(pitch),sum(sum(plot_modes)));

 n=1;
 for p = pitch
    fprintf('Working on pitch %i.\n', p);
    result(n,:) = SP_coupling(p);
    n=n+1;
 end
 plot(pitch,result,'--');

 xlabel('Wavelength [nm]');
 ylabel('Pitch [nm]');
 axis([900 1700 700 2000]);

end

function result = SP_coupling(p)
%
% Version: 2.4
% Latest Date: 4-8-2013
% -- by Chester Hung
%
% Change log v2.4 4-8-2013
%  - improve precision
%
% Procedure:
%   For given metal and pitch size, the program will solve
for the peak
% position of both air and BCB modes. Since the
permittivity of metal also
% depends on the lambda peak, the equation of coupling
free space wave into
% lattice has to be solved iteratively for each mode.
%
% Equation for SPP coupling with lattice momentum:
%
% Free space momentum = lattice SPP modes
% 2pi/Lambda = Sqrt( (k+2pi/P*i)^2 + (2pi/P*j)^2 ) /
%
Real(Sqrt( epi_d*epi_m/(epi_d+epi_m) ))
% Lambda = 2pi *
Real(Sqrt( epi_d*epi_m/(epi_d+epi_m) )) /
%                       Sqrt( (k+2pi/P*i)^2 + (2pi/P*j)^2 )
%
   % ==================== SETTINGS
====================

   global plot_modes lambda pitch eps_m eps_di
defined_mode_index k lambda_axis;

   metal = 'Ag';              % Au/Ag/Al
   pitch = p;              % [nm]
   lambda_range = [900,1700];   % [nm]
   k = 0:0.5:0.5;
    % k vector normalized to 2*pi/P     ex:  0:0.00005:0.5

   [MODE_TYPES, MODE_NUMBERS] = size(plot_modes);

   lambda_axis = 1;
    %    (0) -- frequency [THz]
    %    (1) -- lambda [nm]

   result = zeros(sum(sum(plot_modes)),1);
   result_loop = 1;

   % ==================== PARAMETERS
====================
   c = 2.99792458E8;

   if sum(sum(mod(plot_modes,1))) > 0 ||
sum(sum(plot_modes>1)) > 0
      error('Error: mode is not set correctly, use only 0s and 1s.');
   end

   if mod(lambda_axis,1) > 0 || lambda_axis > 1
      error('Error: lambda_axis is not set correctly.');
   end

   %model = best_fit(lambda_range,metal);
   model = 'Palik_0-2';
   material_file = strcat(metal,'_', model);
%     fprintf('\nUsing %s for %s fitting.\n\n', material_file, metal);

   % Construct metal permittivity vector
   eps_m = load(material_file);
   x_axis = eps_m(:,1);
   eps_m = eps_m(:,2) + 1i*eps_m(:,3);

   lambda = (1:1:max(lambda_range)*2)';
   eps_m = spline(x_axis, eps_m, lambda);

   % ==================== MODE CALCULATION
====================
%     hold on;
   plot_color = ['r', 'g', 'b', 'y', 'm', 'c', 'k'];
   for row = 1:MODE_TYPES    % loop through air to bcb etc.

      if row == 1
         mode = 'air';
         eps_di = 1^2;
         sym_prefix = '.';
```

```
        elseif row == 2
            mode = 'bcb';
            eps_di = 1.45^2;
            sym_prefix = '--';
        elseif row == 3
            mode = 'defined';
            eps_di = defined_mode_index^2;
            sym_prefix = '-.';
        end

        for col = 1:MODE_NUMBERS    % loop through SP1
to SP2 etc.
            if plot_modes(row,col) == 1
                sym = [sym_prefix, plot_color(col)];
                [result1 result2] = plot_all_modes(col,sym);
                result(result_loop) = result1(1);
                result_loop = result_loop+1;
%                 fprintf(' SP%i-%s modes are represented by
%s.\n', col, mode, sym);
            end
        end

    end

    % ===== Plotting parameters =====
%     hold off;
%     xlabel('kx');
%
%     if lambda_axis == 0
%         min_freq = c/(max(lambda)*1e-9)*1e-12;
%         max_freq = c/(min(lambda)*1e-9)*1e-12;
%         axis([0 0.5 min_freq max_freq]);
%         ylabel('frequency [THz]');
%     else
%         axis([0 0.5 min(lambda_range)
max(lambda_range)]);
%         ylabel('lambda [nm]');
%     end

end

%
==========================================
==============================

function model = best_fit(lambda_range, metal)
% This function determines the best material to use in
% certain wavelength range.
%
% Output:
%  - string name for the model, ex. 'Palik', 'CRC', 'JC'
%
% Input:
%  - lambda_range
%  - metal = name of metal
%
    if strcmp(metal, 'Au')
        if min(lambda_range) >= 200 &&
max(lambda_range) <= 2000
            model = 'JC';
        else
            model = 'Palik';
        end
    elseif strcmp(metal, 'Ag')
        if min(lambda_range) >= 1265
            model = 'Palik_1-10';
        elseif max(lambda_range) >= 2100
            model = 'CRC';
        elseif min(lambda_range) >=190
            model = 'JC';
        else
            model = 'Palik_0-2';
        end
    elseif strcmp(metal, 'Al')
        if min(lambda_range) >= 200 && max(lambda_range) <=
2500
            model = 'Palik';
        else
            model = 'CRC';
        end
    else
        error('Error: metal choice is not available.');
    end

end

function [pSP nSP] = plot_all_modes(mode_no,sym)
% This function plots all possible mode combinations given
% a mode number (i+j).
%
% Output:
%  - plot of all possible modes given i+j
%
% Input:
%  - lambda = wavelength range for calculation and plotting
%  - P = pitch
%  - eps_m = epsilon of metal, wavelength dependent
%  - eps_di = epsilon of the dielectric material (ex. air/bcb)
%  - mode_no = sum of i+j
%  - k = momentum
%  - lambda_axis = plot in wavelength (or in frequency)
%  - sym - symbol used for plotting
%

  global k lambda_axis;

  for i = 0:mode_no
      j = mode_no - i;
      pSP = coupling(i+k,j);
      nSP = coupling(i-k,j);
      if lambda_axis == 0
          pSP = c./(pSP01*1e-9)*1e-12;
          nSP = c./(nSP01*1e-9)*1e-12;
      end

      %plot(k,pSP,sym,k,nSP,sym,'LineWidth',2);
  end

end
```

```
function coupled_mode = coupling(kx,ky)
% This function calculates the SPP mode coupled with the
lattice.
% Equation:
% Lambda = 2pi *
Real(Sqrt( epi_d*epi_m/(epi_d+epi_m) )) /
%                        Sqrt( (k+2pi/P*i)^2 + (2pi/P*j)^2 )
%
% Output:
%  - calculated mode using the equation
%
% Input:
%  - lambda = wavelength range for calculation and
plotting
%  - P = pitch
%  - eps_m = epsilon of metal, wavelength dependent
%  - eps_di = epsilon of the dielectric material (ex. air/bcb)
%  - kx = x-direction momentum
%  - ky = y-direction momentum
%

  global lambda pitch eps_m eps_di;

  TOL = 1;           % tolerance on the lambda peak err [nm]
  CYC_MAX = 25;      % max number of loop for each
iteration

  if length(ky) == 1  % in the case where k-vector is placed
along x
     ky = ky + 0*kx; % make ky into a vector for simpler
vector calculation
  else
     kx = kx + 0*ky;
  end

  % Coupled mode iterative calculation
  coupled_mode = zeros(1,length(kx));
  est = round(mean(lambda));
  for l = 1:length(kx)
    err = TOL + 1;
    cyc = 0;

    while err > TOL && est > min(lambda) && est <
max(lambda) && cyc < CYC_MAX
      n = find(lambda == est);
      SPP_mode =
real(sqrt( eps_m(n)*eps_di/(eps_m(n)+eps_di) ));
      %SPP_mode = real(sqrt( eps_di ));
      lattice_mode = sqrt( (2*pi/pitch*kx(l)).^2 +
(2*pi/pitch*ky(l)).^2 );
      coupled_mode(l) = 2*pi*SPP_mode./lattice_mode;

      err = abs(est - coupled_mode(l));
      est = round(coupled_mode(l));
      cyc = cyc + 1;
    end

  end

  % Warning for mode that did not converge
  if cyc >= CYC_MAX || est < min(lambda) || est > max(lambda)
    if kx(1) < kx(2)
       mode = strcat(' SPp', num2str(kx(1)), num2str(ky(1)));
    elseif kx(1) == kx(2)
       mode = strcat(' SP', num2str(kx(1)), num2str(ky(1)));
    else
       mode = strcat(' SPn', num2str(kx(1)), num2str(ky(1)));
    end
%     fprintf('    Warning: %s did not converge.\n',mode);
  end

end
```

Bibliography

1. James, K. SWIR For Target Detection, Recognition, And Identification. *Electronic Military & Defense* 20–21.
2. Sensors Unlimited Sensors Unlimited Micro-SWIR Camera. *UTC Aerospace Systems* (2013).
3. Krishna, S. The Infrared Retina : Ushering in the Fourth Generation of IR Detectors. (2012).
4. Allied Vision Technologies SWIR and LWIR camera technology.
5. Sudharsanan, R., Yuan, P., Boisvert, J., McDonald, P., Isshiki, T., Mesropian, S., Labios, E., and Salibury, M. Single Photon Counting Geiger Mode InGaAs(P)/InP Avalanche Photodiode Arrays For 3D Imaging. *SPIE* **6950**, 69500N–69500N–9 (2008).
6. Martin, T., Brubaker, R., Dixon, P., Gagliardi, M.-A., and Sudol, T. 640x512 InGaAs focal plane array camera for visible and SWIR imaging. *SPIE* **5783**, 12–20 (2005).
7. Harvey, A. R., Beale, J., Greenaway, A. H., Hanlon, T. J., and Williams, J. Technology options for imaging spectrometry. *SPIE* **4132**, 13–24 (2000).
8. Laux, E., Genet, C., Skauli, T., and Ebbesen, T. W. Plasmonic photon sorters for spectral and polarimetric imaging. *Nature Photonics* **2**, 161–164 (2008).
9. Shin, H., Catrysse, P., and Fan, S. Effect of the plasmonic dispersion relation on the transmission properties of subwavelength cylindrical holes. *Physical Review B* **72**, 085436 (2005).
10. Verslegers, L., Catrysse, P., Yu, Z., White, J., Barnard, E., Brongersma, M., and Fan, S. Planar lenses based on nanoscale slit arrays in a metallic film. *Nano letters* **9**, 235–8 (2009).
11. Gupta, N., Ashe, P. R., and Tan, S. Development of a Miniature Snapshot Multispectral Imager. (2010).
12. Gat, N. Imaging Spectroscopy Using Tunable Filters : A Review. **4056**, 50–64 (2000).
13. Verhaegen, M., Lessard, S., and Blais-Ouellette, S. Narrow band SWIR hyperspectral imaging: a new approach based on volume Bragg grating. *SPIE* **8374**, 83740G–83740G–8 (2012).
14. Gao, H., Henzie, J., and Odom, T. W. Direct evidence for surface plasmon-mediated enhanced light transmission through metallic nanohole arrays. *Nano letters* **6**, 2104–8 (2006).
15. Genet, C., and Ebbesen, T. W. Light in tiny holes. *Nature* **445**, 39–46 (2007).
16. Chen, Q., and Cumming, D. R. S. High transmission and low color cross-talk plasmonic color filters using triangular-lattice hole arrays in aluminum films. *Optics express* **18**, 14056–62 (2010).
17. Barnes, W. L., Dereux, A., and Ebbesen, T. W. Surface plasmon subwavelength optics. *Nature* **424**, 824–830 (2003).
18. Barnes, W., Murray, W., Dintinger, J., Devaux, E., and Ebbesen, T. Surface Plasmon Polaritons and Their Role in the Enhanced Transmission of Light through Periodic Arrays of Subwavelength Holes in a Metal Film. *Physical Review Letters* **92**, 1–4 (2004).
19. Muskens, O. L. Local and anisotropic excitation of surface plasmon polaritons by semiconductor nanowires. *Optics Express* **16**, 2144–2148 (2008).
20. Lezec, H. J., Degiron, A., Devaux, E., Linke, R. A., Martin-Moreno, L., Garcia-Vidal, F. J., and Ebbesen, T. Beaming light from a subwavelength aperture. *Science* **297**, 820–2 (2002).
21. Hiskett, P. A., Buller, G. S., Loudon, A. Y., Smith, J. M., Gontiji, I., Walker, A. C., Townsend, P. D., and Robertson, M. K. Performance and design of InGaAs /InP photodiodes for single-photon counting at 1.55 micron. *Applied optics* **39**, 6818–29 (2000).
22. Features, P. PLA-200 & PLA-280 : High Sensitivity Large Area APD Components. 1–2 (2012).
23. Rothman, J. HgCdTe avalanche photodiodes ; a noiseless revolution of photo-detection and imaging. 1–19 (2009).
24. Bailey, S., Mckeag, W., Wang, J., and Jack, M. Advances in HgCdTe APDs and LADAR Receivers. *SPIE Defense Security and Sensors* (2010).
25. XEVA-FPA-2.5-320 SWIR imaging camera for TE4-cooled HgCdTe focal plane arrays (0.85 up to 2.5 µm). (2008).

26. XenICs XS-FPA-1.7-320 SWIR imaging camera for uncooled InGaAs focal plane arrays (0.9 up to 1.7 µm). (2008).
27. Krier, A., and Mao, Y. High performance uncooled InAsSbP / InGaAs photodiodes for the 1 . 8-3 . 4 / xm wavelength range. *Infrared Physics & Technology* **38**, 397–403 (1997).
28. Rogaiskia, A., and Ciupa, R. InGaAs versus HgCdTe for short wavelength infrared applications. *SPIE* **3629**, 328–337 (1999).
29. Gunawan, O., Wang, K., Fallahazad, B., Zhang, Y., Tutuc, E., and Guha, S. High performance wire-array silicon solar cells. *Prog. Photovolt: Res. Appl.* **19**, 307–312 (2011).
30. West, P. R., Ishii, S., Naik, G. V., Emani, N. K., Shalaev, V. M., and Boltasseva, A. Searching for better plasmonic materials. *Laser & Photonics Reviews* **4**, 795–808 (2010).
31. Bruijn, H. E. De, Kooyman, R. P. H., and Greve, J. Choice of metal and wavelength for surface-plasmon resonance sensors : some considerations. *Applied optics* **31**, 440–442 (1992).
32. Ghaemi, H., Thio, T., Grupp, D., Ebbesen, T., and Lezec, H. Surface plasmons enhance optical transmission through subwavelength holes. *Physical Review B* **58**, 6779–6782 (1998).
33. Jiang, Y.-W., Tzuang, D.-C., Ye, Y.-H., Wu, Y.-T., Tsai, M.-W., Chen, C.-Y., and Lee, S.-C. Effect of Wood's anomalies on the profile of extraordinary transmission spectra through metal periodic arrays of rectangular subwavelength holes with different aspect ratio. *Optics Express* **17**, 2631 (2009).
34. FLIR TAU SWIR 15 High Performance Shortwave Infrared Camera.
35. Manissadjian, A., Rubaldo, L., Rebeil, Y., Kerlain, A., Brellier, D., and Mollard, L. Improved IR detectors to swap heavy systems for SWaP. *SPIE* **8353**, 835334–835334–9 (2012).
36. Driggers, R., Holst, G., Reynolds, J., Fanning, J., and Vollmerhausen, R. Infrared detector size: how low should you go? *SPIE* **8355**, 83550O–83550O–9 (2012).
37. Sager, D., Gutsche, C., Prost, W., Tegude, F.-J., and Bacher, G. Recombination dynamics in single GaAs-nanowires with an axial heterojunction: n- versus p-doped areas. *Journal of Applied Physics* **113**, 174303 (2013).
38. Kempa, T. J., Tian, B., Kim, D.-R., Hu, J., Zheng, X., and Lieber, C. M. Single and tandem axial p-i-n nanowire photovoltaic devices. *Nano letters* **8**, 3456–60 (2008).
39. Yoshimura, M., Tomioka, K., Hiruma, K., Hara, S., Motohisa, J., and Fukui, T. Growth and Characterization of InGaAs Nanowires Formed on GaAs(111)B by Selective-Area Metal Organic Vapor Phase Epitaxy. *Japanese Journal of Applied Physics* **49**, 04DH08 (2010).
40. Colombo, C., Heiβ, M., Grätzel, M., and Fontcuberta i Morral, a. Gallium arsenide p-i-n radial structures for photovoltaic applications. *Applied Physics Letters* **94**, 173108 (2009).
41. Lin, A., Shapiro, J. N., Senanayake, P. N., Scofield, A. C., Wong, P.-S., Liang, B., and Huffaker, D. L. Extracting transport parameters in GaAs nanopillars grown by selective-area epitaxy. *Nanotechnology* **23**, 105701 (2012).
42. Senanayake, P., Hung, C.-H., Shapiro, J., Scofield, A., Lin, A., Williams, B., and Huffaker, D. 3D Nanopillar optical antenna photodetectors. *Optics Express* **20**, 25489 (2012).